Supplementary Information

Altered Electronic Structure of Trimetallic FeNiCo-MOF Nanosheets for Efficient Oxygen Evolution

Wenqiang Li,[a#] Heng Zhang,[a,b#] Ka Zhang,[a,b#] Zezhong Cheng,[a] Haipeng Chen,[a] Geng Tan,[a] Xun Feng[a] Liya Wang,[c] Shichun Mu[d*]*

a. *College of Chemistry and Chemical Engineering, Luoyang Normal University, Luoyang, 471934, P. R. China, E-mail: fengx@lynu.edu.cn*

b. *College of Chemistry, Zhengzhou University, Zhengzhou, 450001, P. R. China*

c. *College of Chemistry and Pharmaceutical Engineering, Nanyang Normal University, Nanyang, 473601, P. R. China*

d. *State Key Laboratory of Advanced Technology for Materials Synthesis and Processing, Wuhan University of Technology, Wuhan, 430070, P. R. China, E-mail: msc@whut.edu.cn*

# These authors contributed equally to this work.

1. Experimental Section

1.1 Materials and reagent

Cobalt (II) acetate tetrahydrate ($Co(CH_3COO)_2 \cdot 4H_2O$), nickel (II) acetate tetrahydrate ($Ni(CH_3COO)_2 \cdot 4H_2O$), Ferrous(II) sulfate heptahydrate ($FeSO_4 \cdot 7H_2O$), 1,3,5-Benzenetricarboxylic acid (BTC), N,N-Dimethylformamide (DMF) and ethanol were purchased from Aladdin Industrial Corporation. 5% Nafion solution and Iridium powder (IrO_2, 5wt%) was provided by Sigma Aldrich Corporation. Ni Foam with a thickness of 1.6 mm and 120 ppi (pore per square inch) was purchased from Jia Shide Foam Metal Co., Ltd (Suzhou, China). All chemical reagents were used without any further purification.

1.2 Preparation of trimetallic FeNiCo-based MOF

FeNiCo-MOF was synthesized at room temperature. Firstly, 0.6 mmol $Ni(CH_3COO)_2 \cdot 4H_2O$ (149.3 mg), 0.3 mmol $Co(CH_3COO)_2 \cdot 4H_2O$ (74.7 mg) and 0.1 mmol $FeSO_4 \cdot 7H_2O$ (27.8 mg) were dissolved into 10 ml solution composed of N,N-Dimethylformamid and deionized water (named A solution). And 1 mmol 1,3,5-Benzenetricarboxylic acid (BTC) (210.1 mg) was dissolved in 5 ml solution composed of N, N-Dimethylformamide and deionized water (named B solution). Then, A solutions was quickly poured into B solution under magnetic stirring at room temperature. After 1 h, put one piece of nickel foam into the mixture overnight. Finally, the products $Fe_{0.1}(NiCo)_{0.9}$-MOF (denoted as FeNiCo-MOF) were obtained by washing with DMF to remove surface impurities, and drying at 60°C for 6 hours. Co-MOF or NiCo-MOF are synthesized in the similar method as FeNiCo-MOF except the absent of $Ni(CH_3COO)_2 \cdot 4H_2O$, $FeSO_4 \cdot 7H_2O$ or $FeSO_4 \cdot 7H_2O$.

1.3 Materials characterization

The morphology and structure of the synthesized MOFs are characterized by field emission scanning electron microscopy (FESEM, JSM-6700F), transmission electron microscopy (TEM, JOEL, JEM-2010, Talos F200X), powder X-ray diffractor (XRD, TTR-III), micropore and chemisorption analyzer (Micrometritics, ASAP 2020). The chemical state of the sample was performed on X-ray photoelectron spectroscopy (XPS, ESCALAB 250, UK), the Fourier transform infrared spectroscopy (FT-IR, Nicolet 8700, USA) and confocal Raman microscope (LabRam HR,Horiba Yobin Yvon) with a 30 mW He/Ne laser (633 nm) as the excitation source.

1.4 Electrochemical measurements

Electrochemical measurements were performed with a workstation (CHI 660E, Shanghai, China) in a typical three-electrode configuration consisting of a platinum wire (the counter electrode), saturated calomel electrode (SCE) (the reference electrode) and the active material (the working electrode) in 1.0 M KOH solution. The loads of Co-MOF, NiCo-MOF and FeNiCo-MOF are 2.15, 2.28 and 2.05 mg cm^{-2}, respectively. The measured potentials were given according to the following formula: E(RHE) = E(SCE) + 0.059 × pH + 0.241. Linear sweep voltammetry (LSV) and cyclic voltammetry (CV) measurements were performed to evaluate the OER properties of catalysis. The overpotential (η) was figured out via the following equation: η = E (RHE) - 1.23 V. For comparison, a benchmark IrO_2 catalyst on Ni foam was fabricated by the following steps: 784 μL ethanol, 20 μL Nafion, 196 μL deionized water and 5 mg IrO_2 were mixed to prepare dispersion and sonicated for 30 minute. Finally, a certain of prepared dispersion was add on the NF.

The linear sweep voltammetry (LSV) curves were recorded with a scan rate of 5 mV s^{-1}. The Tafel slope was calculated by fitting the linear portion of the Tafel plots, obtained by using the Tafel equation [η = b log(j) + a]. And all the polarization curves were corrected by the iR-drop compensation. The electrochemical impedance spectroscopy (EIS) was performed to cover the frequency interval from 0.01 Hz to 100 kHz with a 10 mV amplitude.

Electrochemical capacitance measurements were used to determine the active surface area of each catalyst. To estimate the electrochemical active surface area of the electrocatalysts, double-layer capacitance (C_{dl}) was considered in the non-faradaic region (-0.654 ~ -0.714 V vs. RHE) of CVs recorded at different scan rates of 20, 40, 60, 80, 120 and 140 mV s^{-1}. Then, plotting the double-layer charging current at -0.684 V vs. scan rate yields a linear slope, which is equivalent to twice the value of C_{dl}. Finally, the ECSA was obtained through dividing C_{dl} by the specific capacitance of electrode material. Generally, the specific capacitance for flat surface electrodes is 0.06 mF cm^{-2}.

The normalized current density was calculated according to following equation:

j_{ECSA}(normalized) =j/ECSA

where j is the current density, ECSA is electrochemcial active surface area of different electrocatalysts.

The Faradaic efficiency (FE) of OER catalysts is defined as the ratio of the amount of experimentally determined O_2 (ne) to that of the theoretically expected O_2 (nt) from the reaction[1]:

$$FE = \frac{n_e}{n_t}$$

Theoretical amount of O_2 was calculated by applying Faraday Law:
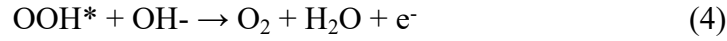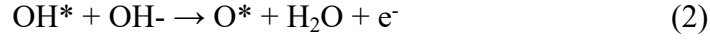
$$n_t = \frac{JAt}{4F}$$

Where J is current density, A is electrode area, t is time in second scale, 4 is number of electron, and F is faraday constant (96,485 C/mol). The Faradaic efficiency is conducted under galvanostatic electrolysis at a current density of -10 mA cm^{-2} over a period of 60 min. Furthermore, quantification of the evolved H_2 was performed by the water drainage method. The experimentally determined volume of H_2 is very close to that of the theoretical value.

2. DFT Computational method

Density functional theory (DFT) calculations were performed using a Dmol3 program package of software Materials Studio 7.0. The Perdew-Burke-Ernzerhof (PBE) function of the generalized gradient approximation (GGA) was used to account for electron exchange and correlation[2]. The computational parameters were self-consistent field (SCF) tolerance 1.0×10^{-7} Ha per atom, energy tolerance 2.0×10^{-7} Ha per atom, maximum force gradient 0.002 Ha Å^{-1}, maximum atomic displacement 0.005 Å, orbital cutoff 4.6 Å and thermal smearing 0.05 Ha for quick convergence. The supercells were relaxed with a $3 \times 3 \times 1$ Monkhorst-Pack k-mesh

The four sequential electron transfer steps, including adsorption steps (i and iii), dissociation steps (ii and iv) and desorption step (v). Considering that the overall water decomposition process requires energy 4.92 eV at the standard conditions, the energy for at least one step in (i–iv) should be larger or equal to 1.23 eV. For the OER in

alkaline environment, the whole process occurs via the following four elementary steps:

$$OH^- + * \rightarrow OH^* + e^- \qquad (1)$$

$$OH^* + OH^- \rightarrow O^* + H_2O + e^- \qquad (2)$$

$$O^* + OH^- \rightarrow OOH^* + e^- \qquad (3)$$

$$OOH^* + OH^- \rightarrow O_2 + H_2O + e^- \qquad (4)$$

The adsorption free energies (ΔG) of OER intermediates can be obtained by $\Delta G_i = \Delta E_i + \Delta ZPE_i - T\Delta S_i$, where i means OH*, O* and OOH*. Li et al. previously reported that $\Delta ZPE - T\Delta S$ are 0.06, 0.37 and 0.44 eV for O*, OH* and OOH*, respectively.[3] Furthermore, the ΔE for OER intermediates was calculated as follow:

$$\Delta E_{OH} = E(OH^*) - E(*) - [E(H_2O) - 1/2E(H_2)]$$

$$\Delta E_O = E(O^*) - E(*) - [E(H_2O) - E(H_2)]$$

$$\Delta E_{OOH} = E(OOH^*) - E(*) - [2E(H_2O) - 3/2E(H_2)]$$

Therefore, the Gibbs free energy changes for the four elementary steps of OER can be expressed as follows:

$$\Delta G_1 = \Delta G_{OH} - eU$$

$$\Delta G_2 = \Delta G_O - \Delta G_{OH} - eU$$

$$\Delta G_3 = \Delta G_{OOH} - \Delta G_O - eU$$

$$\Delta G_4 = 4.92 \text{ eV} - \Delta G_{OOH} - eU$$

Where U is the potential measured against the normal hydrogen electrode (NHE)

at standard conditions. Therefore, the theoretical overpotential (η) for OER can be obtained by the following equation:

$$\eta_{OER} = \max[\Delta G_1, \Delta G_2, \Delta G_3, \Delta G_4]/e - 1.23 \ [V]$$
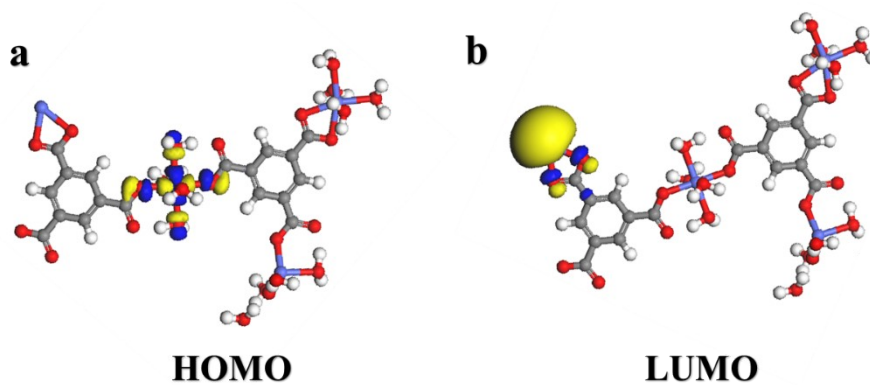
3. Supplementary Figures and Tables

Fig. S1 (a-b) lowest unoccupied molecular orbital (LUMO) and the highest occupied molecular
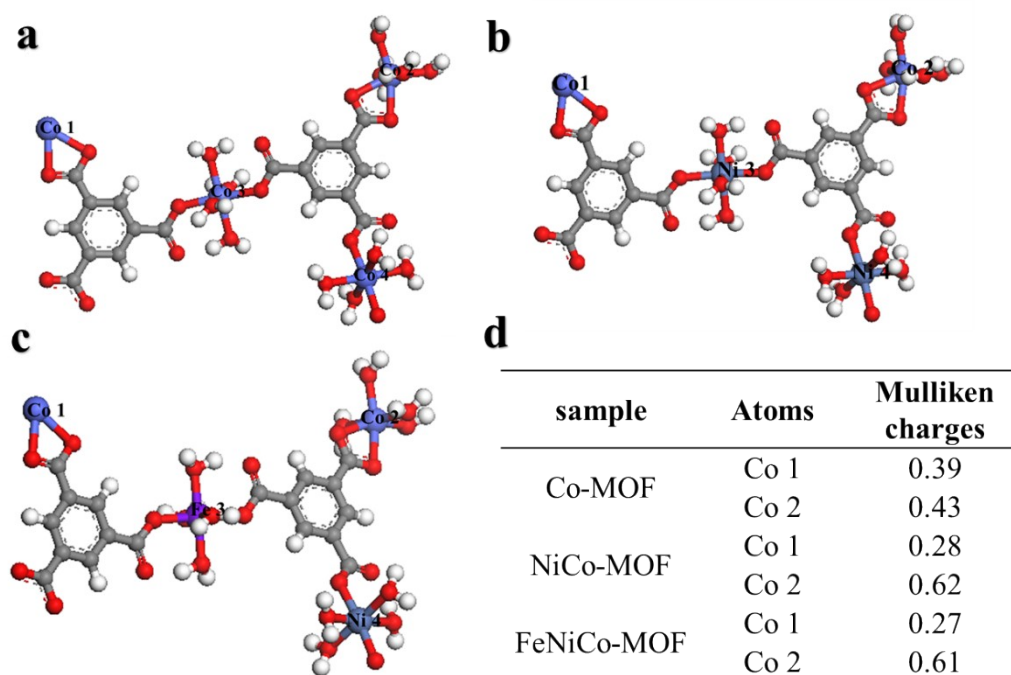
orbital (HOMO) of Co-MOF.

sample	Atoms	Mulliken charges
Co-MOF	Co 1	0.39
	Co 2	0.43
NiCo-MOF	Co 1	0.28
	Co 2	0.62
FeNiCo-MOF	Co 1	0.27
	Co 2	0.61

Fig. S2 (a-c) Simulated Co-MOF, NiCo-MOF and FeNiCo-MOF. (d) Corresponding Mulliken
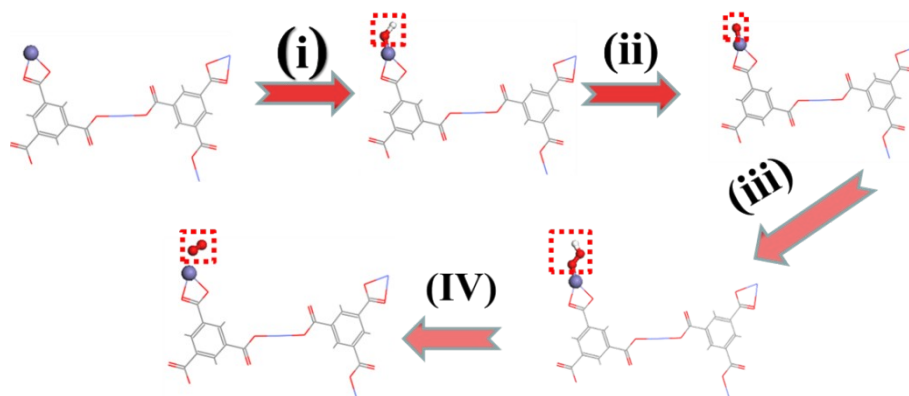
charge analysis of Co1 and Co2 in MOF.

Fig. S3 Typical OER reaction pathway of Co-MOF, including the adsorption, dissociation, and
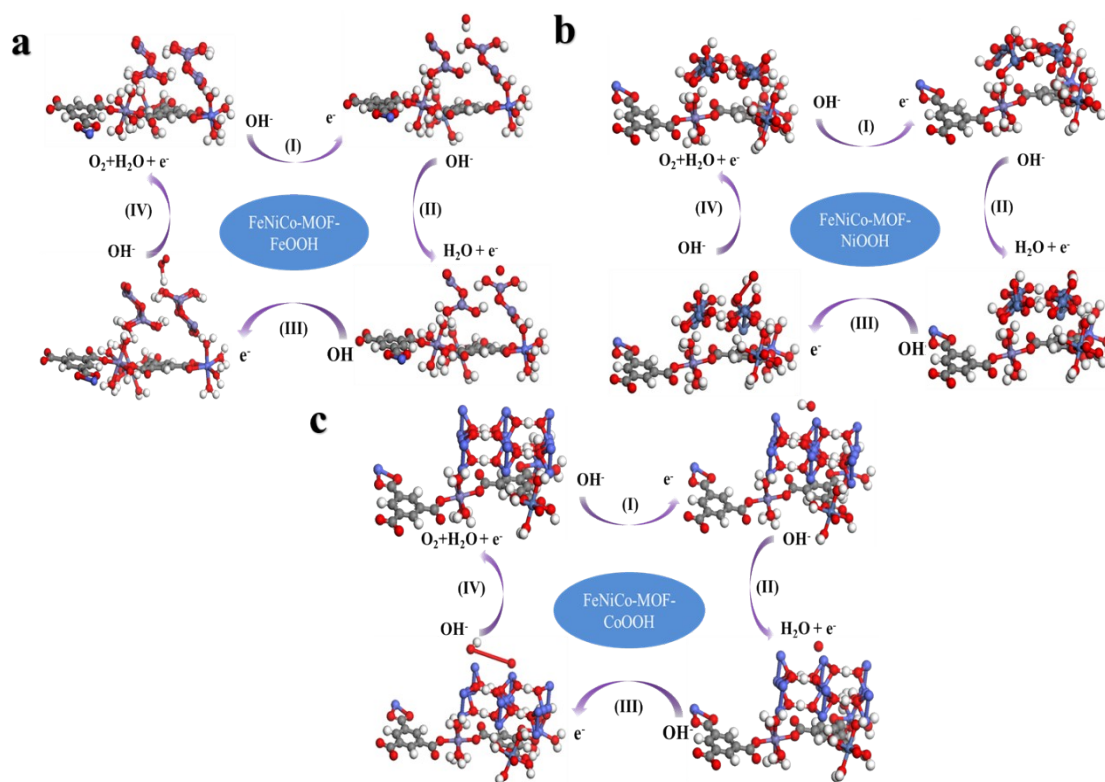
desorption of OER intermediates.

Fig. S4 Theoretical structure models of OH, O, and OOH intermediates adsorbed on the (a)

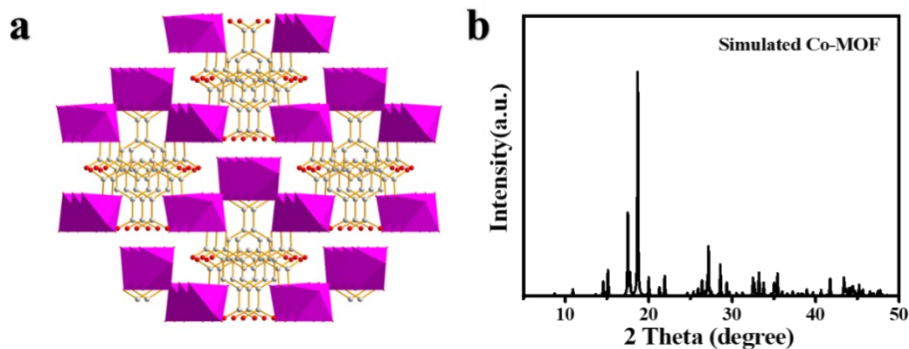FeNiCo-MOF-FeOOH,(b) FeNiCo-MOF-FeOOH, and (c) FeNiCo-MOF-CoOOH.

Fig. S5 Crystal structure (a) and simulated XRD pattern (b) of Co-MOF accessed from CCDC.

The crystal model is obtained based on the previously reported Co-based MOFs (no. 1274034, Cambridge Crystallographic Data Centre)[4], exhibiting a layer MOF structure. First, Ni occupied the lattice sites of Co randomly with the molar ratio of 2:1 (Co:Ni) executed in Diamond software. Then Fe substitute the Ni sites randomly. The simulated XRD pattern is obtained based on the above crystal model.
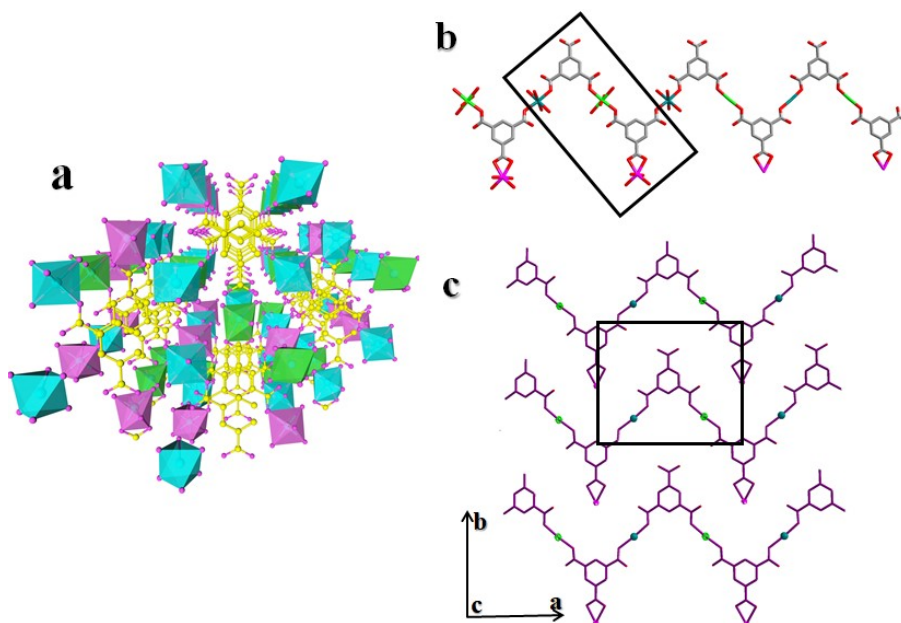

Fig. S6 (a) Crystal structure of FeNiCo-MOF (b) FeNiCo-MOF zigzag chains. The black rectangle singles out the repeating unit. (c) Single FeNiCo-MOF layer representation along the (001) direction.

The infinite zigzag chains aligned along the [101] direction that are formed by the alternation of BTC with Co atoms. As shown in Fig. S6b, when the repeating unit

contains three types atoms (Co,Ni and Fe)[5]. Both BTC molecules in the repeating unit

bind to bridging Ni or Fe atoms in an unidentate mode along the chain, and an additional

Co atom is coordinated in a bidentate fashion by one free carboxylate group on alternate

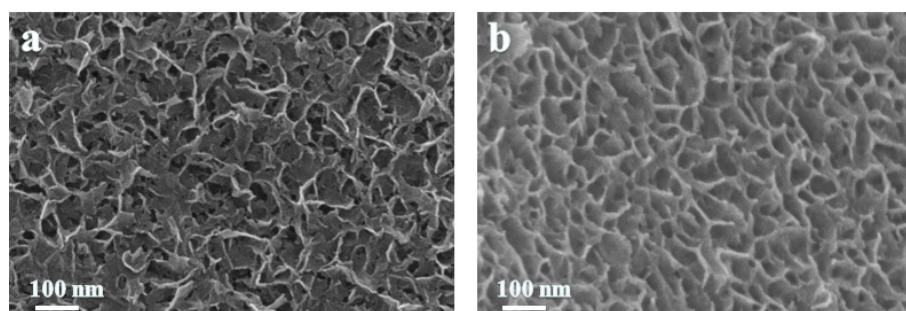BTC molecules, individual zigzag chains stack along the b axis (Fig. S6c).

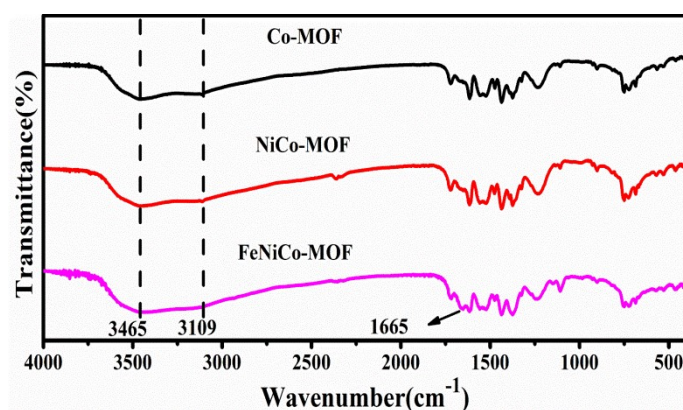Fig. S7 SEM images of (a) Co-MOF and (b) NiCo-MOF.

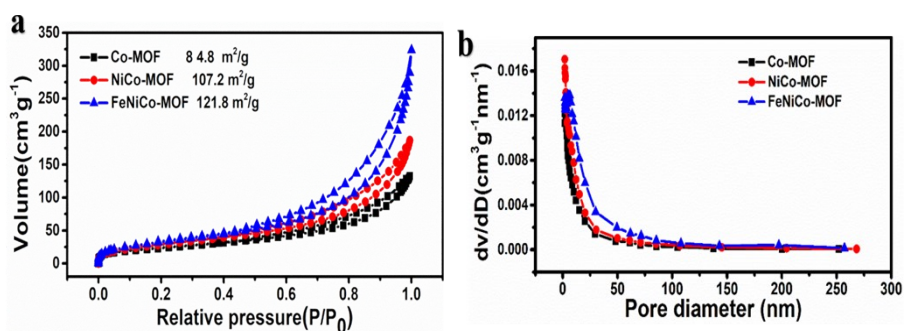Fig.S8　FT-IR of Co-MOF, NiCo-MOF and FeNiCo-MOF

Fig. S9 (a-b)The N$_2$ adsorption-desorption isotherms and pore-size distribution curves of the Co-MOF, NiCo-MOF and FeNiCo-MOF.
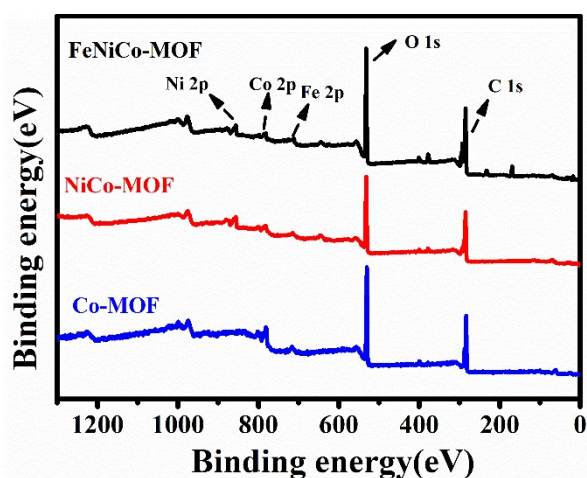

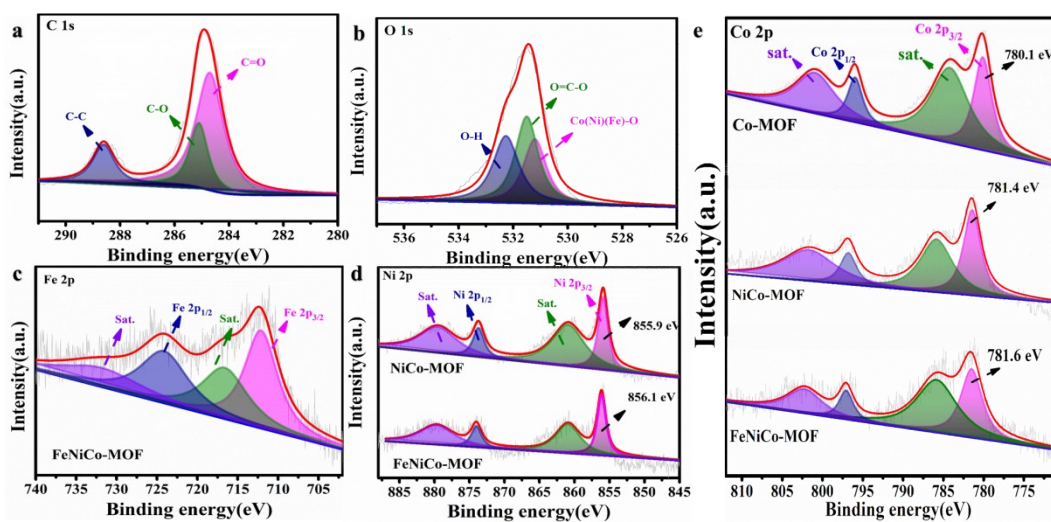Fig. S10 XPS survey pattern of Co-MOF, NiCo-MOF and FeNiCo-MOF.

Fig. S11 (a-c) High-resolution XPS spectra of C 1s, O 1s and Fe 2p for FeNiCo-MOF,

respectively. (d) Ni 2p for NiCo-MOF and FeNiCo-MOF, and (e) Co 2p for Co-MOF, NiCo-MOF,
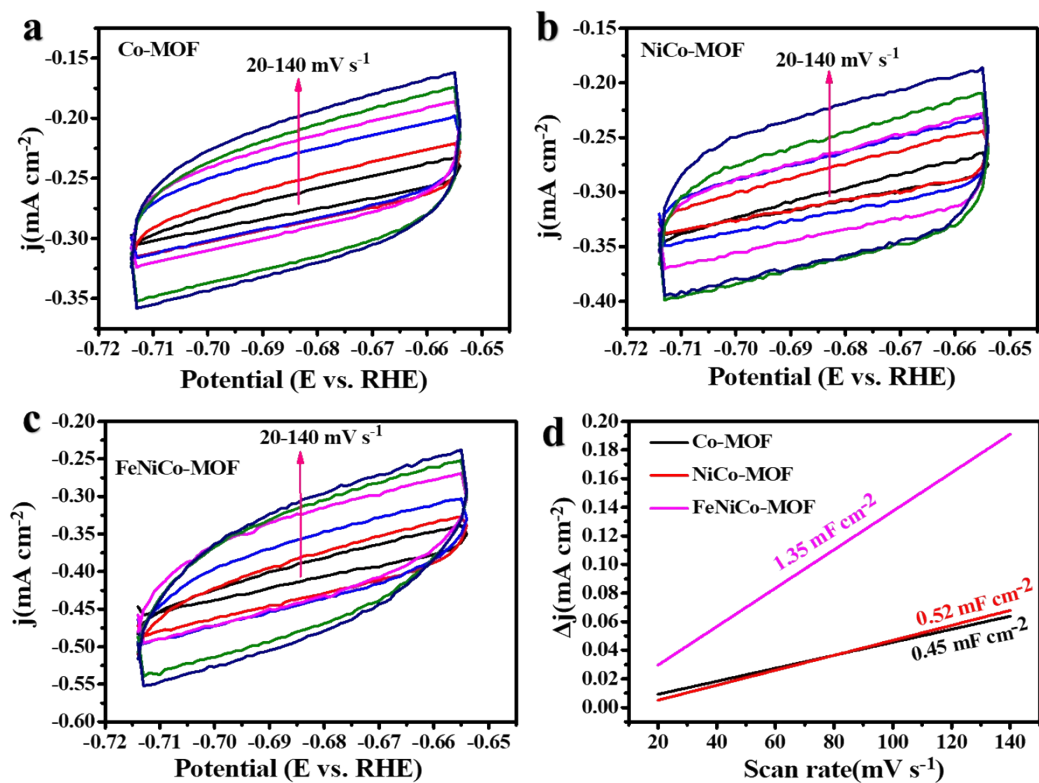
and FeNiCo-MOF.

Fig. S12 CV curve of electrodes recorded at different scan rates of 20, 40, 60, 80, 120 and 140 mVs^{-1} in 1 M KOH solution, for (a) Co-MOF, (b) NiCo-MOF, (c) FeNiCo-MOF, (d) The double layer capacity C_{dl} of synthesized materials.
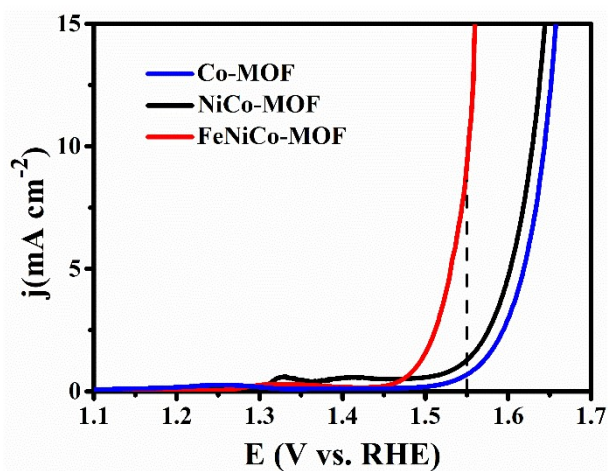

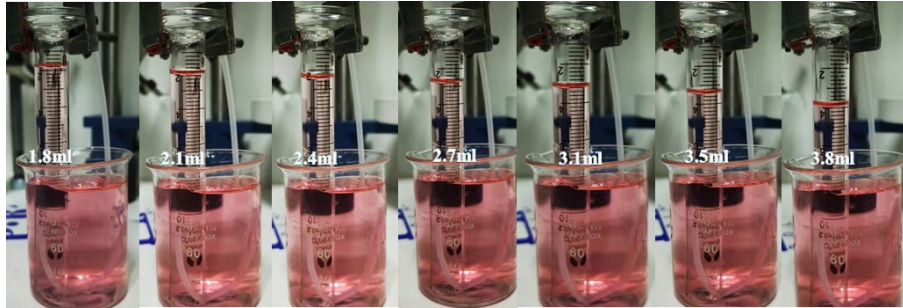Fig. S13 ECSA normalized OER polarization curves of the as-prepared Co-MOF, NiCo-MOF and FeNiCo-MOF electrocatalysts.

Fig. S14 Enlarged digital images of the measuring cyliners displayed and levels of oxygen gas generated at 0, 10, 20, 30, 40, 50, 60 min in 1 M KOH.
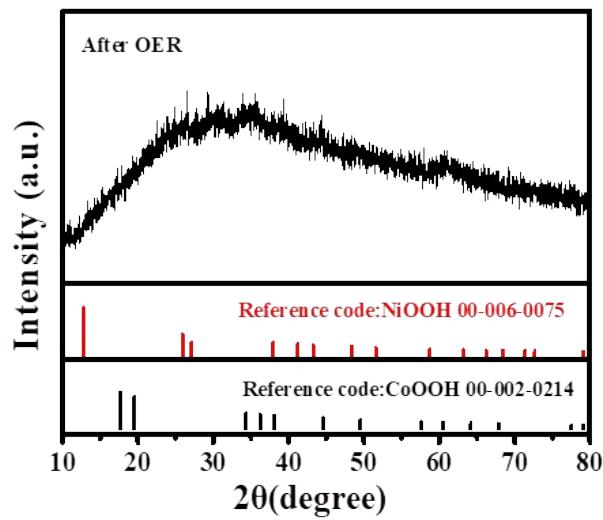

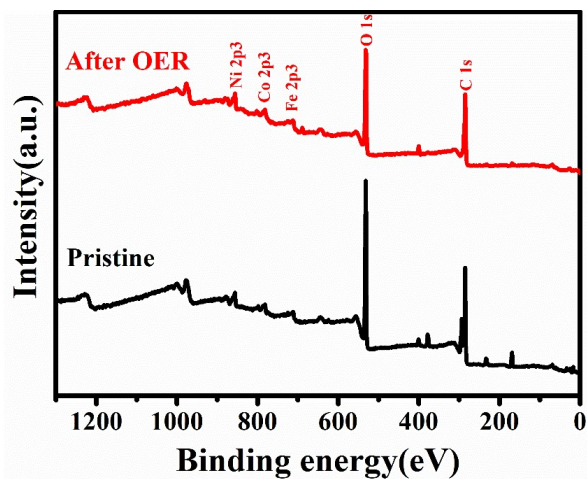Fig. S15 X-ray diffraction patterns of FeNiCo-MOF after OER test

Fig. S16 XPS spectra of the FeNiCo-MOF before and after OER testing.
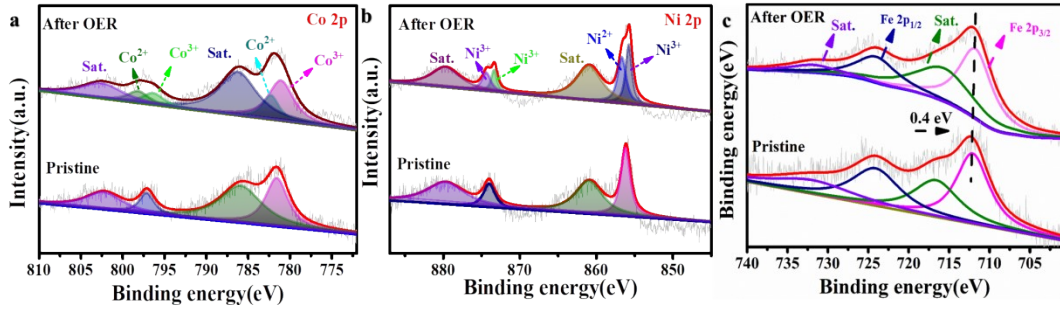
Fig. S17 (a-c) High-resolution XPS spectra of Co 2p, Ni 2p and Fe 2p of the FeNiCo-MOF before
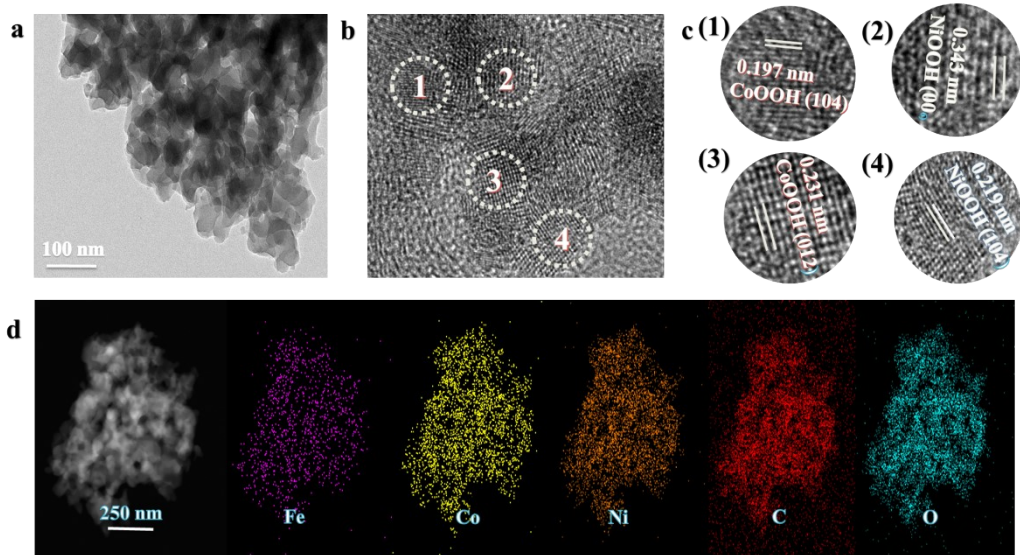
and after OER testing.

Fig. S18 (a) TEM images, (b-c) HRTEM images. (d) The EDS mappings of the FeNiCo-MOF

after OER test.

Table S1. Comparison of the OER activity for FeNiCo-MOF with several recently reported electrocatalysts

Materials	Substrate	$\eta_{10/\text{mA cm}^{-2}}$ (mV)	Tafel slope (mV dec^{-1})	Electrolyte	Ref.
FeNiCo-MOF	**NF**	**239**	**42.4**	**1 M KOH**	**This work**
Fe-MOF/NF	NF	253	74.8	1 M KOH	[7]
Fe$_2$Co-MOF	GCE	339	36.2	1 M KOH	[8]
Co-MOF-5 fibers	CC	240	120	0.1 M KOH	[9]
CoFe-MOF	NF	265	44	0.1 M KOH	[10]
CoNiFe LTHs	GCE	262	88.1	1 M KOH	[11]
FeCoMOF-EH	GCE	231	42	1 M KOH	[12]
CuO/TiO$_2$@MOF-5	NF	263	91	0.1 M KOH	[13]
CoS$_x$/Co-MOF	NF	280	83	1 M KOH	[14]
Co-MOF/AB	GCE	280	51	0.1 M KOH	[15]
Ni-MOF@CNT	NF	370	138.2	1 M KOH	[16]
Ni-MOF/LDH	NF	220	36	1 M KOH	[17]
Fe-Ni LDH/MOF	CC	255	24	1 M KOH	[18]
Fe(OH)$_3$@Co-MOF-74	GCE	292	44	1 M KOH	[19]
Fe@NiCo-MOF HNSs	GCE	244	48.6	1 M KOH	[20]
Ru@NiCo-MOF HPNs	GCE	284	78.8	1 M KOH	[21]
Co/Ni(BDC)$_2$TED@CF	CF	260	76.2	1 M KOH	[22]
CuCo-MOF	CFP	340	173.5	1 M KOH	[23]

Table S2. Atomic percentages obtained from ICP-MS analyses of MOFs removed from corresponding MOF/NF electrodes

MOF	Atomic%			Ratio
	Fe	Ni	Co	
FeNiCo-MOF	1.46	8.1	5.2	1:5.3:3.3
After ADT test	0.84	4.7	3.3	1:5.4:3.7

After the OER test, the dissolved concentration of Fe, Ni and Co in reacted solution was 14.8, 79.8 and 47.7 ppb, respectively.

Reference

1. J. C. Li, C. Zhang, T. Zhang, Z. H. Shen, Q. W. Zhou, J. Pu, H. J. Ma, T. H. Wang, H. G. Zhang, H. M. Fan, Y. Y. Wang and H. X. Ma, *Chem. Eng. J*, 2020, **397**, 11.

2. J. P. Perdew, K. Burke and M. Ernzerhof, *Phys. Rev. Lett*, 1996, **77**, 3865-3868.

3. Y. C. Yao, S. L. Hu, W. X. Chen, Z. Q. Huang, W. C. Wei, T. Yao, R. R. Liu, K. T. Zang, X. Q. Wang, G. Wu, W. J. Yuan, T. W. Yuan, B. Q. Zhu, W. Liu, Z. J. Li, D. S. He, Z. G. Xue, Y. Wang, X. S. Zheng, J. C. Dong, C. R. Chang, Y. X. Chen, X. Hong, J. Luo, S. Q. Wei, W. X. Li, P. Strasser, Y. E. Wu and Y. D. Li, *Nature. Catalysis*, 2019, **2**, 304-313.

4. M. C. Shi, Q. Wang, J. W. Hao, H. H. Min, H. R. You, X. M. Liu and H. Yang, *Dalton. transactions*, 2020, **49**, 14115-14122.

5. A. Nowacka, P. Briantais, C. Prestipino and F. Xamena, *Cryst. Growth. Des*, 2019, **19**, 4981-4989.

6. A. Mesbah, P. Rabu, R. Sibille, S. Lebegue, T. Mazet, B. Malaman and M. Francois, *Inorg. Chem*, 2014, **53**, 872-881.

7. Z. Wang, J. Xu, J. H. Yang, Y. H. Xue and L. M. Dai, *Chem. Eng. J*, 2022, **427**, 131498.

8. M. L. Gu, S. C. Wang, C. Chen, D. K. Xiong and F. Y. Yi, *Inorg. Chem*, 2020, **59**, 6078-6086.

9. R. Madhu, S. S. Sankar, K. Karthick, A. Karmakar, S. Kumaravel and S. Kundu, *Inorg. Chem*, 2021, **60**, 9899-9911.

10. Z. H. Zou, T. T. Wang, X. H. Zhao, W. J. Jiang, H. R. Pan, D. Q. Gao and C. L. Xu, *ACS Catal*, 2019, **9**, 7356-7364.

11. R. Yu, D. M. Liu, M. Y. Yuan, Y. Wang, C. Q. Ye, J. Li and Y. K. Du, *J. Colloid. Interf. Sci*, 2021, **602**, 612-618.

12. J. Y. Tian, F. L. Jiang, D. Q. Yuan, L. J. Zhang, Q. H. Chen and M. C. Hong, *Angew. Chem. Int. Edit*, 2020, **59**, 13101-13108.

13. A. Jabbar, M. Fiaz, S. Rani, M. N. Ashiq and M. Athar, J. Inorg. Organomet. P, 2020, **30**, 4043-4052.

14. H. Z. Xu, K. Ye, K. Zhu, J. L. Yin, J. Yan, G. L. Wang and D. X. Cao, *Inorg. Chem.*

Front., 2020, **7**, 2602-2610.

15. R. K. Tripathy, A. K. Samantara and J. N. Behera, *Dalton. T*, 2019, **48**, 10557-10564.

16. T. V. M. Sreekanth, G. R. Dillip, P. C. Nagajyothi, K. Yoo and J. Kim, *Appl. Catal. B-Environ*, 2021, **285**, 119793.

17. J. M. Huo, Y. Wang, L. T. Yan, Y. Y. Xue, S. N. Li, M. C. Hu, Y. C. Jiang and Q. G. Zhai, *Nanoscale*, 2020, **12**, 14514-14523.

18. Z. Gao, Z. W. Yu, F. Q. Liu, C. Yang, Y. H. Yuan, Y. Yu and F. Luo, *ChemSusChem*, 2019, **12**, 4623-4628.

19. J. L. Xing, K. L. Guo, Z. H. Zou, M. M. Cai, J. Du and C. L. Xu, *Chem Commun*, 2018, **54**, 7046-7049.

20. C. Li, X. J. Li, Z. Y. Zhao, F. L. Li, J. Y. Xue, Z. Niu, H. W. Gu, P. Braunstein and J. P. Lang, *Nanoscale*, 2020, **12**, 14004-14010.

21. D. M. Liu, H. Xu, C. Wang, H. Y. Shang, R. Yu, Y. Wang, J. Li, X. C. Li and Y. K. Du, *Inorg. Chem*, 2021, **60**, 5882-5889.

22. D. J. Li, Q. H. Li, Z. G. Gu and J. Zhang, *J. Mater. Chem. A*, 2019, **7**, 18519-18528.

23. Q. C. Liu, J. H. Chen, F. Yu, J. N. Wu, Z. Y. Liu and B. H. Peng, *New. J. Chem*, 2021, **45**, 16714-16721.